Supplementary Information: Visualizing thickness-dependent magnetic textures in few-layer $Cr_2Ge_2Te_6$

Andriani Vervelaki,[1] Kousik Bagani,[1] Daniel Jetter,[1] Manh-Ha Doan,[2] Tuan K. Chau,[2] Boris Gross,[1] Dennis Christensen,[3] Peter Bøggild,[2] and Martino Poggio[1,4]

[1]*Department of Physics, University of Basel, 4056 Basel, Switzerland*

[2]*Department of Physics, Technical University of Denmark, 2800 Kongens Lyngby, Denmark*

[3]*Department of Energy Conversion and Storage, Technical University of Denmark, 2800 Kongens Lyngby, Denmark*

[4]*Swiss Nanoscience Institute, University of Basel, 4056 Basel, Switzerland*

SUPPLEMENTARY NOTE 1: ATOMIC FORCE MICROSCOPY

The SOL scanning probe is capable of performing conventional non-contact mode AFM. This allows for a topographic mapping of the measured CGT flake in parallel to SSM. Supplementary Figure 1a shows a greyscale optical image of the investigated CGT flake with lines indicating corresponding AFM line-cuts plotted below. Supplementary Figure 1b shows the topography of the flake gathered via SOL AFM by dynamically adjusting the tip-sample spacing to keep a constant frequency shift of -23 Hz correlated to 150 nm tip-sample distance. The AFM image shows the regions of different thickness across the flake. A surface roughness of 300 pm allows us to measure single atomic layer transitions of CGT with $\Delta z = 0.7\,\mathrm{nm}$. Supplementary Figure 1c shows corresponding line cuts extracted from the AFM image showing the respective layer transitions across the flake.

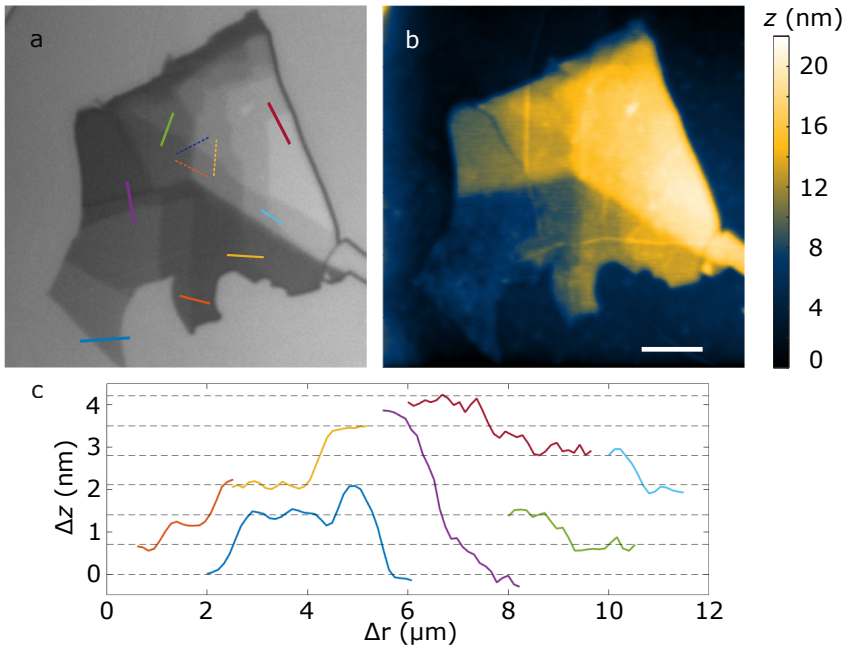

Supplementary Figure 1: **Sample topography.** Greyscale optical image of the investigated CGT flake (a). Solid lines indicate measured layer transitions shown in (c). (b) Topography of the CGT flake measured with the SOL, and (c) corresponding AFM line scan layer transitions with dashed lines indicating 0.7 nm CGT layer transitions.

SUPPLEMENTARY NOTE 2: SQUID CHARACTERISTICS

The SQUID is characterized and operates in a semi-voltage biased circuit. Its current I_{SQ} is measured by a Magnicon series SQUID array amplifier as shown in the inset of Supplementary Figure S2a. Sweeping the bias voltage V_{b} at various out-of-plane applied magnetic fields $\mu_0 H_z$ creates I-V curves as shown in Supplementary Figure 2a and a full set gives a map of the magnetic response $\frac{1}{\mu_0}\frac{\mathrm{d}I_{\mathrm{SQ}}}{\mathrm{d}H_z}$ as shown in Supplementary Figure 2b. The observed modulation yields the SQUID's effective area with an approximate diameter of 270 nm. The SQUID response reaches up to $\frac{1}{\mu_0}\frac{\mathrm{d}I_{\mathrm{SQ}}}{\mathrm{d}H_z}$ = 3000 $\mu\mathrm{AT}^{-1}$ and persists beyond $\mu_0 H_{\mathrm{z}} > 250$ mT. In spatial scans, the SQUID DC signal resolves magnetic signatures down to 1 μT.

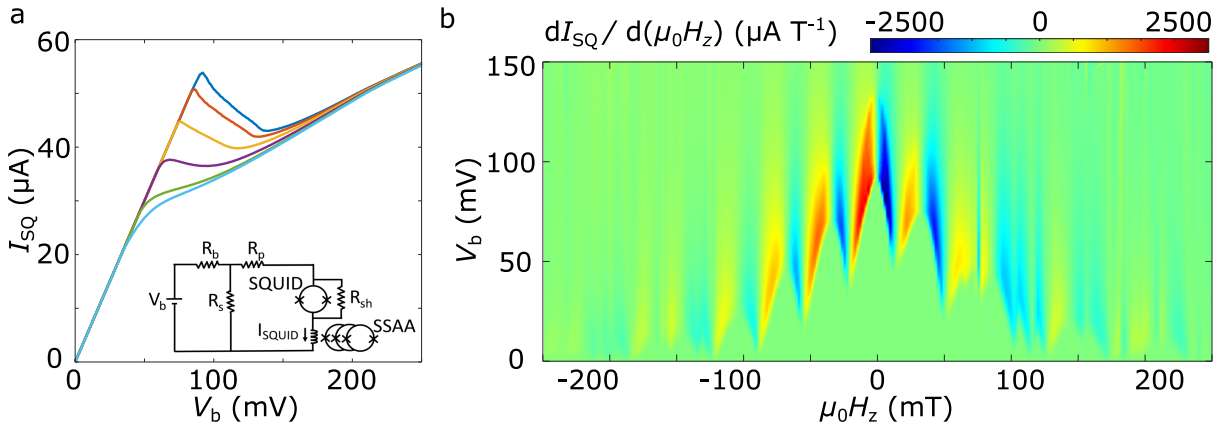

Supplementary Figure 2: **SQUID characterization.** (a) Circuit scheme and current-voltage curves at applied out-of-plane magnetic fields $\mu_0 H_z$ of -2 mT, -6 mT, -10 mT, -14 mT, -18 mT and -22 mT. (b) Map or the SQUID's magnetic response $\frac{1}{\mu_0}\frac{\mathrm{d}I_{\mathrm{SQ}}}{\mathrm{d}H_z}$ in a field range of -250 mT to 250 mT.

SUPPLEMENTARY NOTE 3: MAGNETIC IMAGING

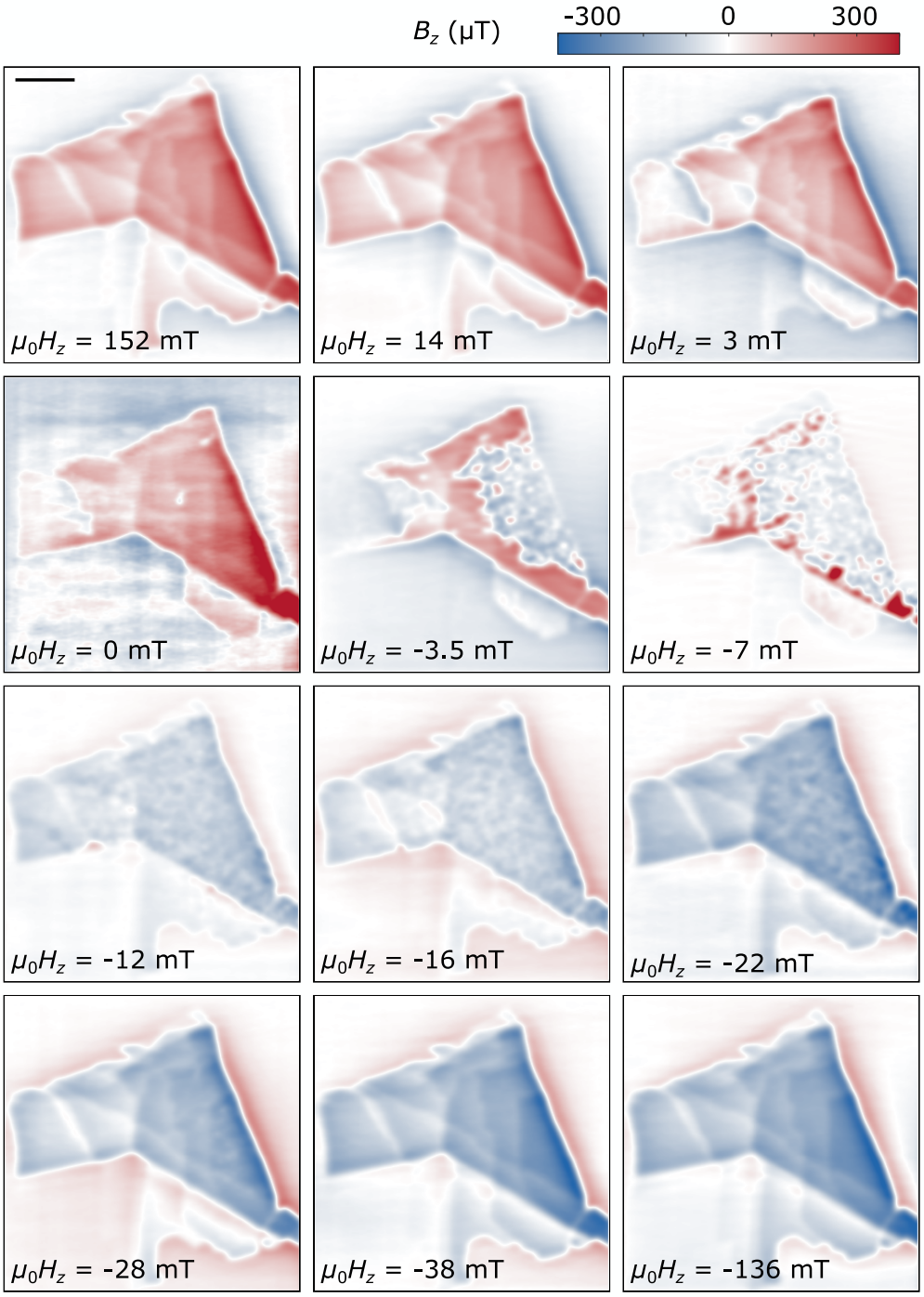

Supplementary Figure 3: **Scanning images sweeping** H_z. Selection of images of the magnetic field $B_z(x, y)$ with progressively decreasing H_z. The scale bar in the top-left corresponds to $5\,\mu$m.

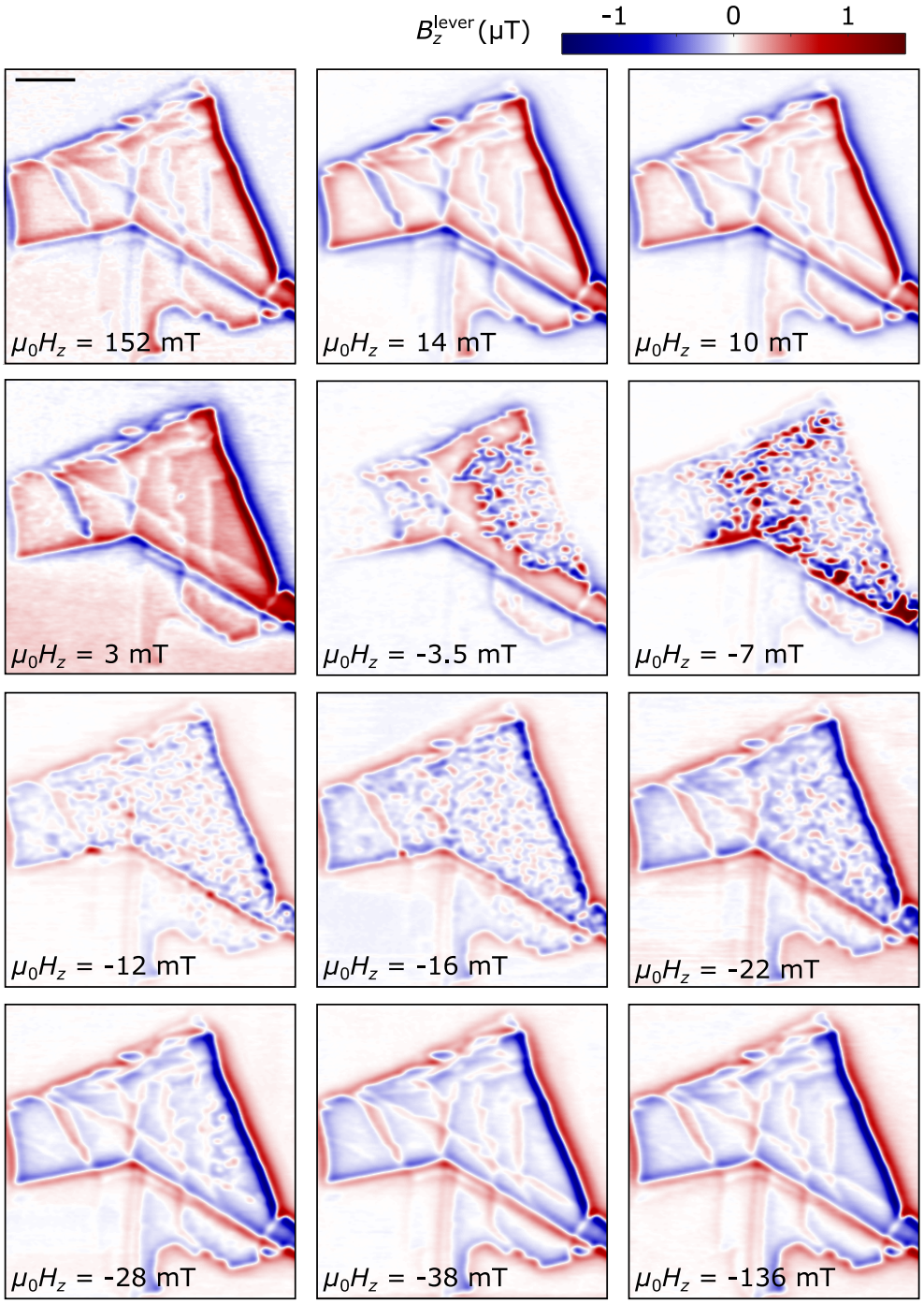

Supplementary Figure 4: **Scanning images sweeping** H_z. Selection of images of the magnetic field gradient signal $B_z^{\text{lever}}(x, y)$ with progressively decreasing H_z. The scale bar in the top-left corresponds to 5 μm.

We image a pristine CGT flake by measuring the DC out-of-plane magnetic field B_z and $B_{\text{lever}} \propto \mathrm{d}B_z/\mathrm{d}z$. We imaged the flake over a full hysteresis loop of out-of-plane applied magnetic field, in order to distinguish layer-dependent switching behavior and domain formation. Supplementary Figure 3 and 4 show a selection of B_z and B_{lever} images of a downward sweep of the applied out-of-plane field H_z. Supplementary Figure 5 shows local hysteresis curves for regions of different thickness throughout the CGT flake. In order to obtain curves related to local magnetic behavior, $B_z(x, y)$ is averaged over a region of constant thickness and then plotted as a function of H_z.

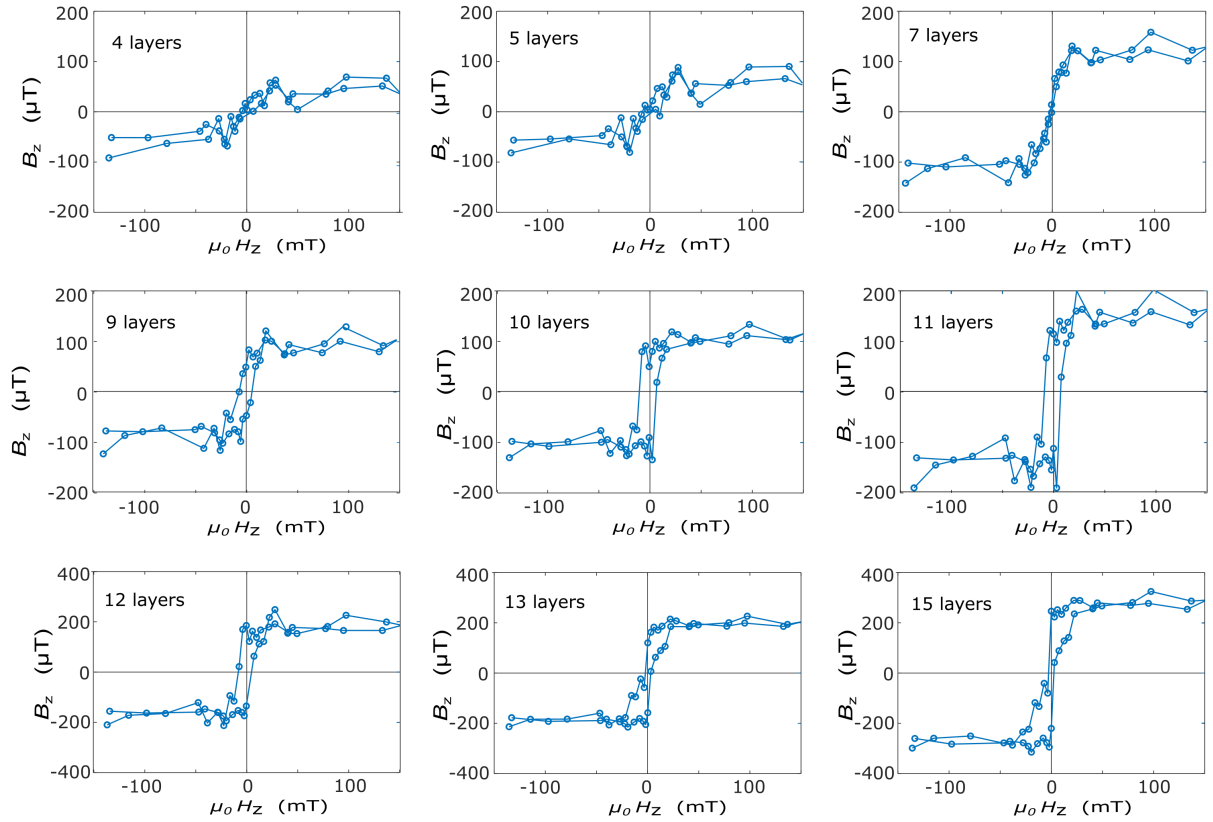

Supplementary Figure 5: **Evolution of hysteresis loop with thickness.** Selection of B_z averaged over a region of constant thickness, indicated on the plot, plotted as a function of out-of-plane applied field H_z.

SUPPLEMENTARY NOTE 4: $\mathbf{B}_z(x,y)$ AND $\mathbf{M}_z(x,y)$ RECONSTRUCTION

Fourier-space image processing is employed to filter noise, remove artifacts from the scanning process, and reconstruct the magnetization from measurements of the stray magnetic field. We use a Hanning window to filter high-frequency noise and line scan artifacts. The sample magnetization $\mathbf{M}(x,y)$ is reconstructed from $B_z(x,y)$ maps via a backpropagation in k-space $\mathbf{M}(k_x,k_y) = \mathbb{A}^{-1}\mathbf{B}_z(k_x,k_y)$. Given a thin and fully polarized magnetic flake, we assume a homogeneous magnetization direction confined to a 2D plane. The flake generates a magnetic field with out-of-plane component B_z measured in a plane at spacing z. A magnetization fully pointing out-of-plane is defined in k-space as $\mathbf{M}_z = \alpha\mathbf{B}_z/k$ with $\alpha = 2e^{kz}/\mu_0$ considering the propagation of the field from its source to the measured plane.

In order to compare to our measurments, we calculate the $B_z(x,y)$ map in a plane at spacing z for a saturated $M_z(x,y)$ via an equivalent forward-propagation. We define the magnetization of the flake as confined to a 2D plane in the exact shape of the flake with $M_z(x,y) = n(x,y)\, M_z^{\text{layer}}$, where $n(x,y)$ is the number of magnetic layers in each particular region and M_z^{layer} is the magnetization per layer. The resulting simulated stray magnetic field, $B_z^{\text{sim}}(x,y)$ is shown in Supplementary Figure 6 and matches with the measured $B_z(x,y)$ shown in Figure 1c.

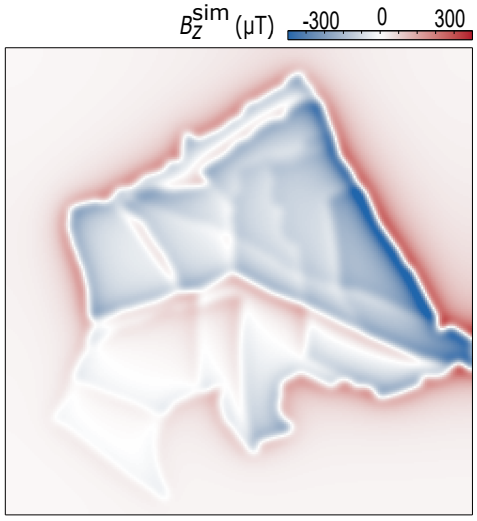

Supplementary Figure 6: **Simulated stray field map.** $B_z^{\text{sim}}(x,y)$ in a plane at spacing $z = 200$ nm for a saturated $M_z(x,y)$.

SUPPLEMENTARY NOTE 5: MICROMAGNETIC SIMULATIONS

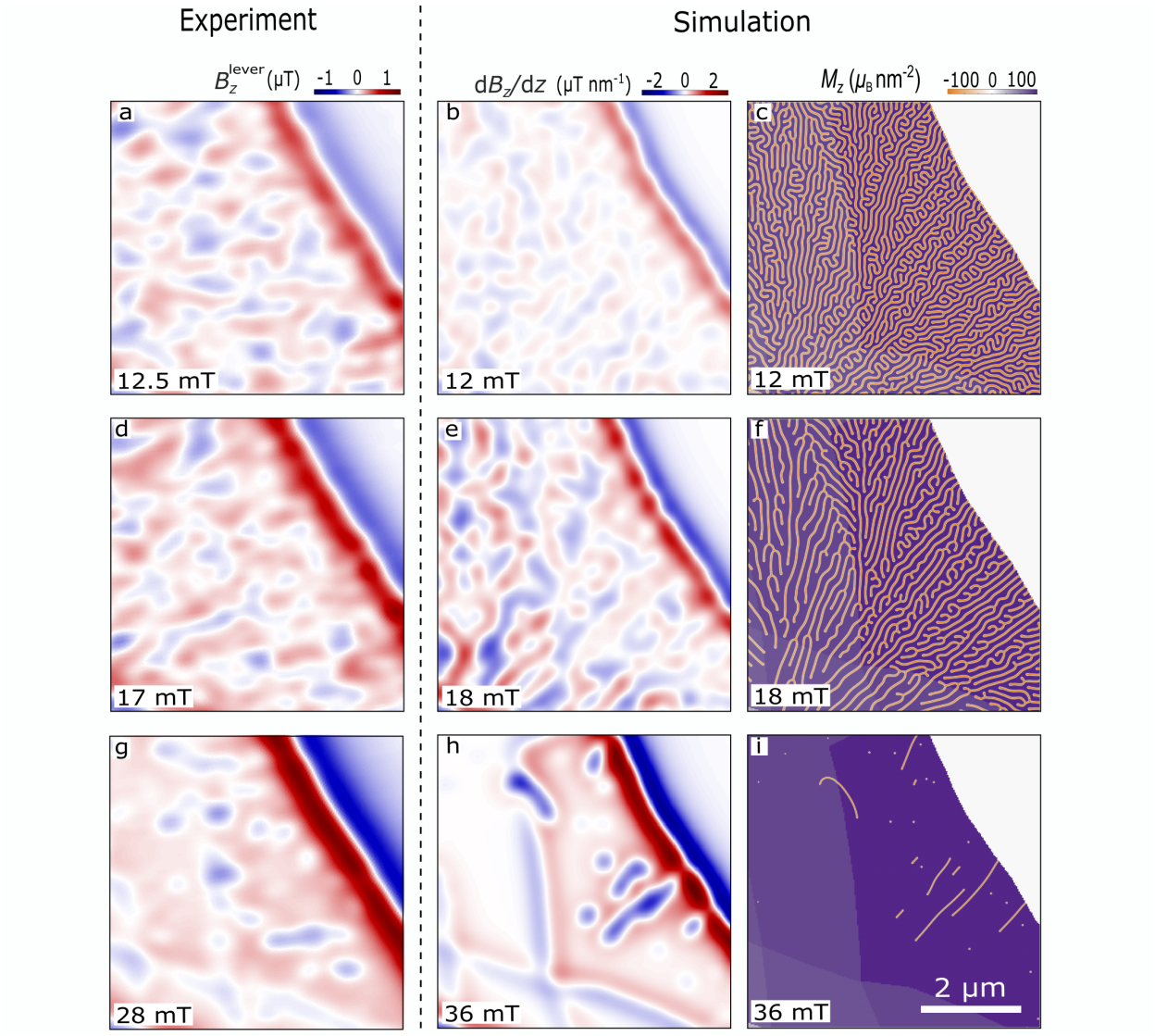

Supplementary Figure 7: **Evolution of magnetic domains under increasing H_z for 13-15 layers.** (a) $B_z^{\text{lever}}(x, y)$ measured at $\mu_0 H_z$ = 12.5 mT over the 13 to 15-layer-thick region of the sample indicated by green and purple dots in Figure 1a, together with (b) the corresponding simulation of $\frac{\mathrm{d}B_z(x,y)}{\mathrm{d}z}$ and (c) $M_z(x, y)$ under similar $\mu_0 H_z$. (d-f) and (g-i) show again the measured $B_z^{\text{lever}}(x, y)$ together with corresponding simulations under externally applied $\mu_0 H_z$ = 17 mT and $\mu_0 H_z$ = 28 mT respectively.

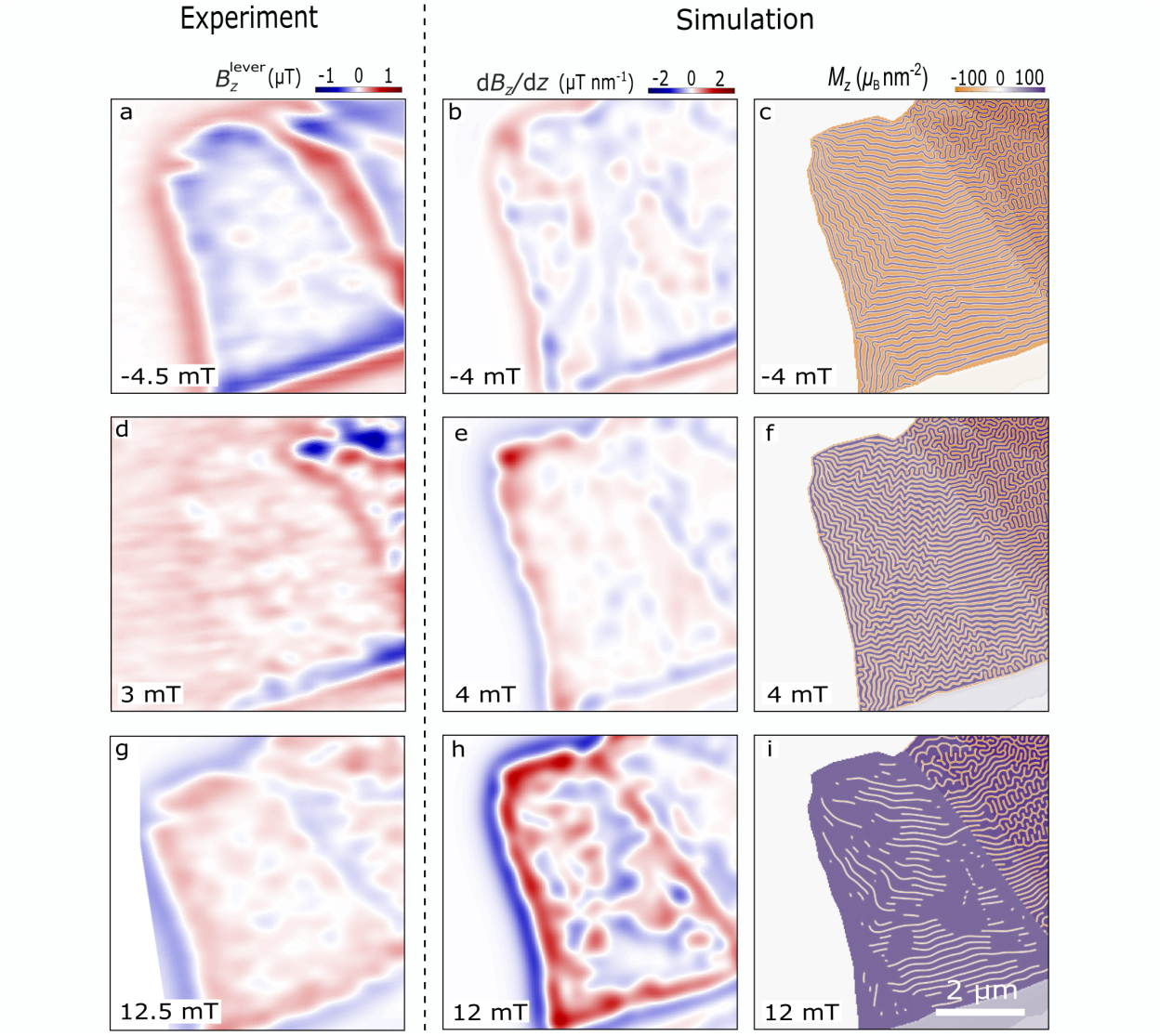

Supplementary Figure 8: **Evolution of magnetic domains under increasing H_z for 7-9 layers.** (a) $B_z^{\text{lever}}(x, y)$ measured at $\mu_0 H_z = -4.5$ mT over the 7 to 9-layer-thick region of the sample indicated by green and purple dots in Figure 1a, together with (b) the corresponding simulation of $\frac{\mathrm{d}B_z(x,y)}{\mathrm{d}z}$ and (c) $M_z(x, y)$ under similar $\mu_0 H_z$. (d-f) and (g-i) show again the measured $B_z^{\text{lever}}(x, y)$ together with corresponding simulations under externally applied $\mu_0 H_z = 3$ mT and $\mu_0 H_z = 12.5$ mT respectively.

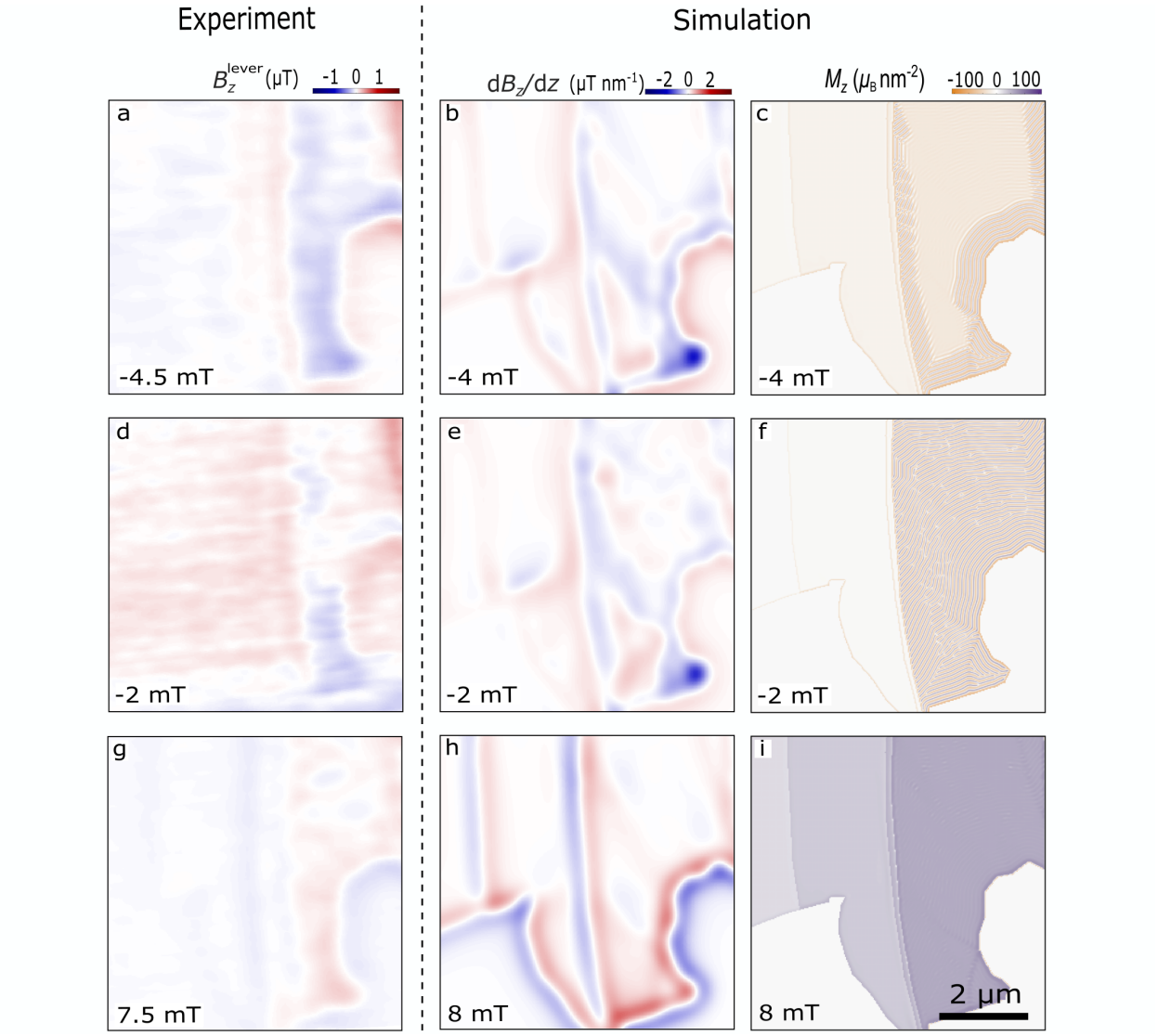

Supplementary Figure 9: **Evolution of magnetic domains under increasing H_z for 3-5 layers.** (a) $B_z^{\text{lever}}(x, y)$ measured at $\mu_0 H_z = -4.5$ mT over the 3 to 5-layer-thick region of the sample indicated by green and purple dots in Figure 1a, together with (b) the corresponding simulation of $\frac{\mathrm{d}B_z(x,y)}{\mathrm{d}z}$ and (c) $M_z(x, y)$ under similar $\mu_0 H_z$. (d-f) and (g-i) show again the measured $B_z^{\text{lever}}(x, y)$ together with corresponding simulations under externally applied $\mu_0 H_z = -2$ mT and $\mu_0 H_z = 7.5$ mT respectively.

The simulated evolution of the magnetization texture under increasing H_z for different areas of the measured CGT flake is presented in Supplementary Figure 7, 8 and 9. The experimentally measured $B_z^{\mathrm{lever}}(x, y)$ is compared with the simulated $dB_z(x, y)/dz$ and $M_z(x, y)$ for selected applied out-of-plane fields H_z. Due to roughly one magnetically inactive layer found in the experiment, the simulation only considers the number of magnetically active layers. As depicted in Figure 3, the simulated spin texture of CGT changes with the number of layers. Upon decreasing the number of layers, labyrinth domains evolve into parallel stripe domains. As depicted in Supplementary Figure 10 the underlying spin texture changes mostly due to the increasing effect of shape-anisotropy and to a smaller extent due to the decrease in the magnetocrystalline anisotropy K_{u} and the intralayer exchange stiffness A_{ex}. The stripe domains within 15 layer CGT show a Néel-type domain wall on the top and bottom outer layers that progressively transitions into a Bloch-type wall towards the middle layer. As thickness is decreased, the stripes have an increased in-plane magnetization component since the shape anisotropy also increases. Also, the stripes are topologically trivial as shown in Supplementary Figure 10 for 7 and 5 layers. However, there is still some small progressive change in the helicity of the domain walls from the top to the bottom layer. Such effects are inferred from simulations, but cannot be directly imaged by our SSM technique due to a lack of spatial resolution and the fact that we measure B_z rather than all vectorial components of the local magnetization.

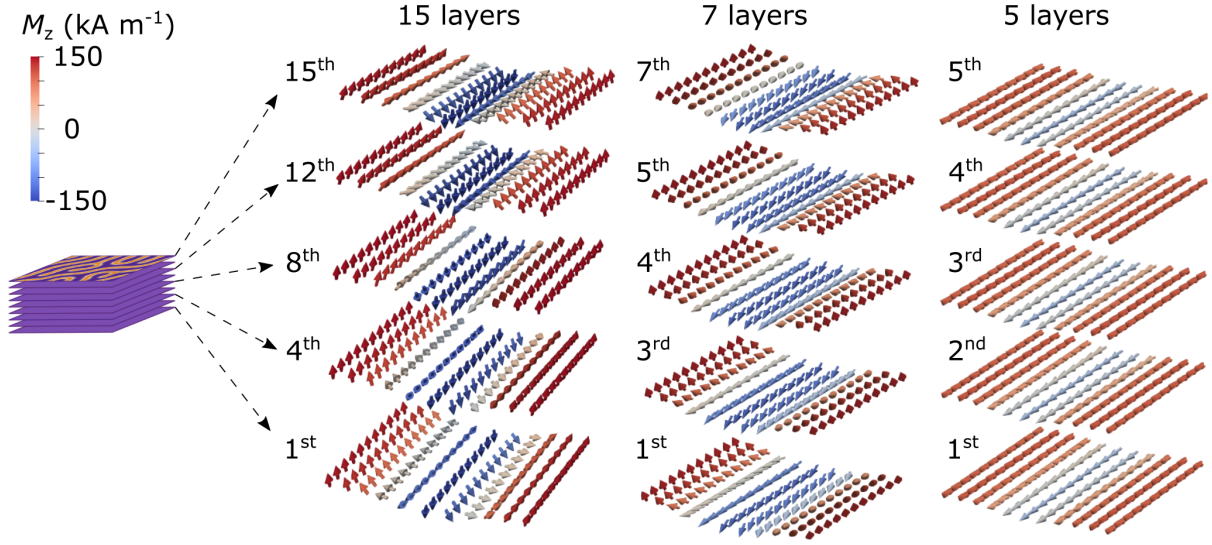

Supplementary Figure 10: Simulated spin texture of magnetic stripe domains for three thicknesses of the flake.